Hongliang Hua[1]
School of Aeronautics and Mechanical Engineering,
Changzhou Institute of Technology,
Changzhou, Jiangsu 213032, China;
School of Mechanical Engineering,
Nanjing University of Science and Technology,
Nanjing 210094, China
e-mail: huahl123@126.com

Jie Song
School of Mechanical Engineering,
Nanjing University of Science and Technology,
Nanjing 210094, China
e-mail: sj0501510127@126.com

Jingbo Zhao
School of Automotive Engineering,
Changzhou Institute of Technology,
Changzhou, Jiangsu 213032, China
e-mail: zhaojb@czu.cn

Zhenqiang Liao
School of Mechanical Engineering,
Nanjing University of Science and Technology,
Nanjing 210094, China
e-mail: zqliao1013@126.com

Sensor-Less Grasping Force Control of a Pneumatic Underactuated Robotic Gripper

The primary motivation of this study is to develop a sensor-less, easily controlled, and passively adaptive robotic gripper. A back-drivable pneumatic underactuated robotic gripper (PURG), based on the pneumatic cylinder and underactuated finger mechanism, is presented to accomplish the above goals. A feedforward grasping force control method, based on the learned kinematics of the underactuated finger mechanism, is proposed to achieve sensor-less grasping force control. To enhance the grasping force control accuracy, a state-based actuating force modeling method is presented to compensate the hysteresis error which exists in the transmission mechanism. Actuating force control experiment is performed to validate the effectiveness of the state-based actuating pressure modeling method. Results reveal that compared with the non-state-based modeling method, the proposed state-based actuating force modeling method could reduce the modeling error and control error by about 37.0% and 77.2%, respectively. Results of grasping experiments further reveal that grasping force could be accurately controlled by the state-based feedforward control model in a sensor-less approach. Adaptive grasping experiments are performed to exhibit the effectiveness of the sensor-less grasping force control approach.
[DOI: 10.1115/1.4056955]

Keywords: grasping, robotic gripper, force control, mechanism design, grasping and fixturing

1 Introduction

Robotic gripper is a fundamental component of the robot to achieve grasping operations and has wide applications in agricultural picking [1–3], food packing [4–7], and minimally invasive surgery [8–10]. Grasping force control is an essential requirement for the robotic gripper to achieve adaptive and nondestructive grasping. On the one hand, the finger mechanism could adapt to the object adaptively by grasping force control and achieve object grasping. On the other hand, robotic gripper could achieve nondestructive object grasping by limiting the grasping force in a safe range [11,12]. How to sense and control the grasping force has become a hot topic in robotic grasping community.

A. Grasping force sensing

Grasping force sensing is the first step in grasping force control. According to the sensing principle, existing grasping force sensing methods could be classified into two kinds: (1) Fingertip force sensor. Extensive research work has been devoted to the development of fingertip force sensors, such as tactile arrays [13,14], miniature three-axis force sensors [15,16], flexible printed circuit boards [17], to cite a few. The fingertip force sensor has the advantage of measuring the grasping force directly. Therefore, it has better generality in different applications. However, the fingertip force sensor contacts with the object directly, it is easier to be contaminated and even damaged, which could affect the stability of grasping force measurement. In addition, there is no guarantee that the object will contact every part of the finger mechanism in practical grasping operation. Therefore, the finger mechanism requires several haptic sensors to enhance the stability of the grasping force sensing. This could greatly aggravate the complexity of the sensing and control; (2) Self-sense. To avoid the damage of the force sensor, another approach is to allocate the force sensor remotely with respect to the finger mechanism. During the grasping, the grasping force will be transmitted from the fingertip to the force sensor. By studying the transmission characteristic of the grasping force under a certain grasping mechanism, the grasping force could be sensed by a remote sensing element in a self-sense manner [18–21]. Previous studies have revealed that the self-sense approach has the potential to reduce the number of the force sensor in a grasping system and achieve sensor-less adaptive grasping.

B. Actuating method

At present, micro servo motor has been widely adopted to control the grasping motion and force of the underactuated robotic gripper [22,23]. Due to the rigidity of the servo motor as well as the transmission mechanism, grasping force control often exists overshoot during the grasping [22], which could lead to the potential risk of object damage. To solve this problem, miniature series elastic actuating (SEA) method has been developed to achieve compliant actuating and grasping. According to the output motion type, the miniature SEA has covered rotary [24] and linear SEA [25]. Previous study has revealed that the SEA actuated robotic gripper could exhibit a series of ideal grasping characteristics, such as back-drive, adaptive grasping, and non-overshoot [18]. Previous study reveals that the main reason for the non-overshoot characteristic of the SEA actuated robotic grasping is due to the existence of the elastic element in the actuating mechanism. During the grasping process, the grasping force will experience a compliant buffer process and improve the control performance. As a result, the grasping force control exhibits a non-overshoot characteristic.

Inspired by the series elastic actuating method, we have observed that the pneumatic actuator has an inherent series elastic actuating characteristic due to its compressible actuating medium, which in most cases is air. Currently, there are three main types of pneumatic actuators. Those are pneumatic elastomer actuator [7,26,27], pneumatic muscle [28–30], and pneumatic cylinder [31]. Among them, pneumatic elastomer actuator and pneumatic muscle are mainly applied to the soft finger mechanism and manipulator fields,

[1]Corresponding author.

Contributed by the Mechanisms and Robotics Committee of ASME for publication in the Journal of Mechanisms and Robotics. Manuscript received June 8, 2022; final manuscript received February 13, 2023; published online March 8, 2023. Assoc. Editor: Kwok Wai Samuel Au.

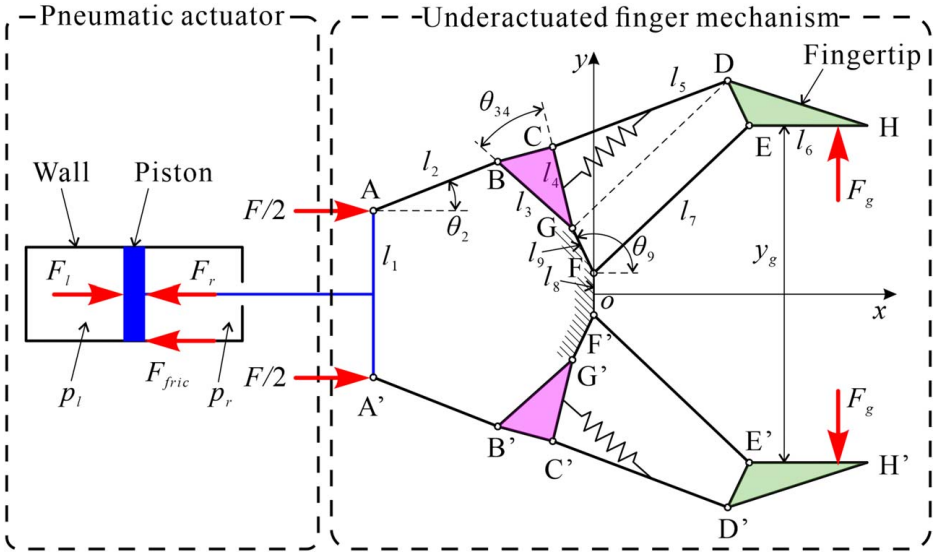

Fig. 1 Transmission mechanism of the PURG

respectively. Due to the nonlinear characteristic of the soft materials, the pneumatic elastomer actuator and pneumatic muscle exhibit an inherent time-varying hysteresis characteristic during loading and unloading process, which could affect the force control accuracy and even the control stability [27,32]. Compared with pneumatic elastomer actuator and muscle, the pneumatic cylinder has a relatively stable hysteresis characteristic due to its stable structure and material. This characteristic of the pneumatic cylinder makes it more beneficial for accurate modeling and control.

C. Research motivation

The primary motivation of this research work is to develop a back-drivable pneumatic underactuated robotic gripper (PURG) to achieve adaptive object grasping by grasping force control in a sensor-less approach, and study the grasping characteristic of the proposed PURG. As depicted in Fig. 1, an underactuated finger mechanism [18] is utilized to endow the gripper with ideal grasping generality. A linear pneumatic cylinder is adopted to actuate the underactuated finger mechanism in a feedforward approach. The maximum transmission ratio between the actuating and grasping force is about 0.33, and the PURG could exhibit an ideal back-drivable characteristic. In this way, the grasping force could transmit to the actuating space efficiently and be sensed and controlled by the pneumatic actuating system in a feedforward approach. Therefore, the overall configuration of the PURG is sensor-less, which could benefit for reducing hardware and control complexity.

The main contributions of this study, include four aspects: (1) A back-drivable pneumatic underactuated robotic gripper based on double-acting pneumatic cylinder as well as its pneumatic control system is designed and fabricated; (2) A feedforward grasping force control method, which based on the learned kinematics of the underactuated finger mechanism, is proposed to achieve sensor-less grasping force control; (3) A state-based actuating force modeling method is proposed to compensate the hysteresis error which exists in the transmission mechanism to enhance the grasping force control accuracy; (4) Sensor-less grasping experiments are performed to reveal the feedforward grasping force control characteristic of the gripper.

In the following sections, the hardware description of the PURG is described in Sec. 2. Section 3 presents the description of the state-based actuating force modeling method. Actuating force control experiments are performed to verify the effectiveness of the actuating force model. Sensor-less grasping force control strategy is introduced in subsequent. In Sec. 4, experimental platform is developed to verify the effectiveness of the proposed method. Grasping experiments are then performed to evaluate the grasping performance of the PURG. Conclusions are given in Sec. 5.

2 Hardware Description

2.1 Sensor-Less Grasping Force Control Mechanism. The overall transmission scheme of the pneumatic underactuated robotic gripper is depicted in Fig. 1. To endow the underactuated robotic gripper with larger grasping range and adaptive grasping ability, a metamorphic four-bar mechanism [18] has been adopted. As shown in Fig. 1, when the linkage AA' is actuated to move linearly along the x-axis, the actuating force F of the pneumatic cylinder will be transmitted to the linkage DEH and D'E'H' through the linkages AB, A'B', BCG, B'C'G', and the four-bar mechanisms GDEF and G'D'E'F'. Due to the stable transmission characteristic of the linkage mechanism, there exists a specific relationship between the actuating force F and the grasping force F_g. As a result, the grasping force F_g could be sensed and controlled by the actuating force F based on the force transmission characteristic of the finger mechanism in a sensor-less approach. Therefore, the fingertips DEH and D'E'H' are designed as sensor-less in the present study. The sensor-less design has the advantages of reducing hardware and control complexity of the PURG.

2.2 Finger Mechanism. For the finger mechanism, four kinds of transmission schemes are commonly used, those are linkage [19,33–35], tendon/cable [14,36,37], gear drives [38], and belt [39]. Among these transmission schemes, the linkage finger mechanism is characterized as simple structure, high transmission efficiency, and stable. As described in Sec. 2.1, the grasping force sense and control rely on the stability of the force transmission characteristic of the finger mechanism. Therefore, the linkage type finger mechanism is adopted in this study. The design considerations and key parameters are introduced in our previous work [18]. To reduce the friction of the finger mechanism, micro sliding bearing, which is made of Teflon material and has a low friction, is embedded into the joints of the finger mechanism, as shown in Fig. 2. In this way, the overall finger mechanism could exhibit a low friction characteristic, which is negligible in modeling.

2.3 Pneumatic Actuator. Our previous study has revealed that by introducing an elastic element to the transmission link between the actuating and grasping space, the grasping force control will exhibit a non-overshoot characteristic, which is quite

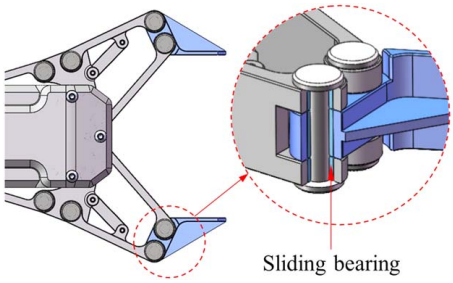

Fig. 2 Design of the underactuated finger mechanism

favorable in adaptive grasping applications [18,19,24,25]. Inspired by the elastic actuating principle, pneumatic cylinder is utilized in this study to actuate the underactuated finger mechanism. Since the actuating medium of the pneumatic cylinder is compressible air, which has an inherent elastic characteristic without the requirement of additional elastic structure. This characteristic of the pneumatic cylinder could result in a more simplified hardware of the PURG. Among the available pneumatic cylinder products, there are double-acting and single-acting pneumatic cylinders. The single-acting pneumatic cylinder has an internal spring, which could produce a restoring force for restoring motion of the finger mechanism. However, due to the fabrication factors, the spring always has a nonlinear stiffness, which could disturb the modeling accuracy of the actuating force. Compared with the single-acting pneumatic cylinder, the double-acting pneumatic cylinder has a relatively simple structure, which is beneficial to reduce the complexity of the actuating force modeling. Therefore, a miniature double-acting pneumatic cylinder is utilized to actuate the finger mechanism in the present design. The bore and trip of the cylinder are 16 mm and 30 mm, respectively. The selected pneumatic cylinder could produce an actuating force of about 78.4 N under 0.5 MPa pressure.

2.4 Overall Configuration. As shown in Fig. 3, the control system of the proposed gripper consists of an air compressor, servo valve, pressure regulator, buffer gas tank, and microcontroller. The pressure of the air compressor is divided into two pipelines, one for actuating pressure p_l and the other for providing restoring pressure p_r. The actuating pressure p_l is controlled by the servo valve through an external voltage instruction u. The servo valve has a full-scale sensitivity, repetition accuracy, and hysteresis of 0.2%, ±0.5%, and 0.5%, respectively. The restoring pressure p_r is adjustable by the pressure regulator to provide different restoring

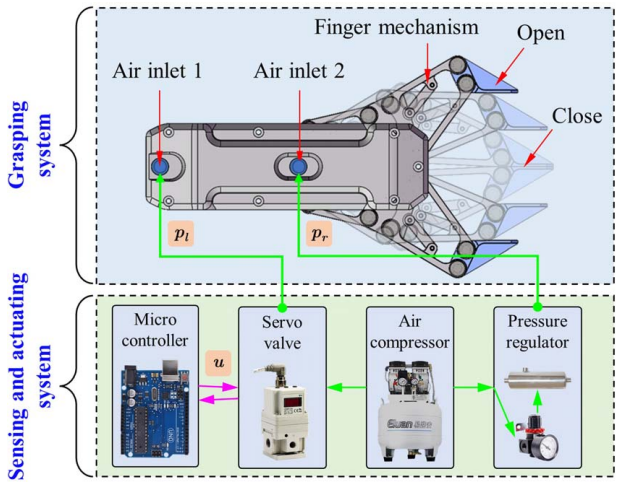

Fig. 3 Physical prototype and its control system

speeds of the cylinder. As the piston moves, restoring pressure p_r will be disturbed to affect the hysteresis characteristic of the actuating force. Therefore, a buffer gas tank is adopted to reduce the effect of restoring pressure p_r on the control accuracy of the actuating pressure p_l. The volume of the buffer gas tank in the present design is 350 ml.

3 Modeling

3.1 Target Actuating Force Modeling. For a given grasping force F_g, the target actuating force of the pneumatic cylinder could be model as

$$F = \frac{F_g}{r_f} \tag{1}$$

where $r_f = F_g/F$ denotes the force transmission ratio. In our previous work [18], a kinematic simulation of the grasping process of the underactuated finger mechanism is performed to obtain the force transmission characteristic between the actuating and grasping space. During the grasping process, r_f exhibits a nonlinear behavior with respect to the grasping range y_g, as depicted in Fig. 4. It reveals that during the grasping process, r_f will increase first and then decrease. r_f will achieve a maximum of 0.33 when $y_g = 56.3$ mm. Taking into consideration the fitting accuracy and simplicity, the simulated discrete sequence of r_f is fitted into a fifth-ordered polynomial function as

$$\begin{aligned} r_f = &-5.1\times10^{-11}y_g^5 + 8.5\times10^{-9}y_g^4 \\ &- 5.9\times10^{-7}y_g^3 + 6.7\times10^{-6}y_g^2 + 1.4\times10^{-3}y_g + 0.3 \end{aligned} \tag{2}$$

As shown in Fig. 4, the fitted r_f, that is Eq. (2), is in accordance with the simulated one globally.

3.2 Experimental Platform for Pneumatic Modeling. To identify the relation between the actuating force F and the pressure p_l, an experimental platform is established as shown in Fig. 5. An Arduino UNO microcontroller is utilized to control the actuating pressure p_l through a servo valve. As the actuating pressure p_l increases, the cylinder will produce extension motion and its piston rod will apply an actuating force F on the force gauge, which has a measuring range of 100 N, full-scale nonlinearity 0.1%, repeatability 0.05%, and hysteresis 0.05%. The model identification experiment includes two steps: (1) set appropriate restoring pressure p_r; (2) adjust the actuating pressure p_l between 0.1 MPa and 0.58 MPa with a step of 0.01 MPa linearly and measure the actuating force F. The interval between each step is 3 s to ensure that the control could be completed. Taking into consideration the hysteresis characteristic of the pneumatic cylinder, the above loading and unloading process has been performed five rounds.

Two sets of typical measured response of the actuating force F and actuating pressure p_l are displayed in Fig. 6. In Fig. 6(*a*), the

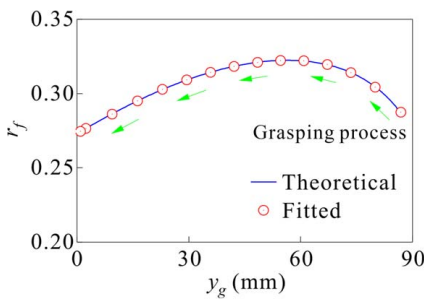

Fig. 4 Force transmission characteristic under different grasping states

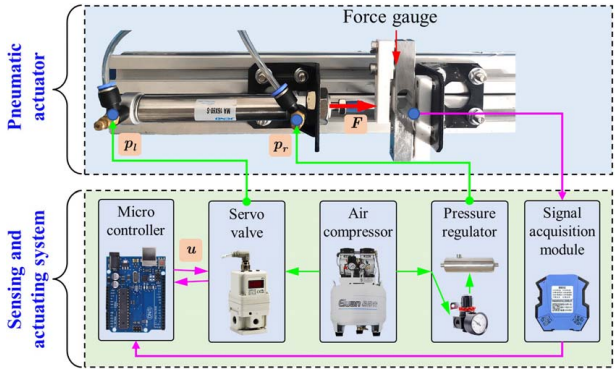

Fig. 5 Experimental platform for model identification

p_r is set as 0.1 MPa. As p_l increase from 0.1 MPa to 0.58 MPa, the actuating force increase to 88.5 N approximately. Since the restoring pressure p_r is set as 0.1 MPa, the cylinder could not produce restoring motion when the actuating pressure decreases to the atmospheric. In Fig. 6(*b*), the p_r is set as 0.2 MPa. As p_l increase from 0.1 MPa to 0.58 MPa, the actuating force increases to 70.8 N abruptly. Compare Figs. 6(*a*) and 6(*b*), it could be found that due to the increment of the restoring pressure p_r, the maximum of the actuating force F will decrease accordingly. Figure 6(*b*) reveals that the cylinder could produce retraction and extension motion when actuating pressure is lower than 0.17 MPa and higher than 0.22 MPa. This means that $p_r = 0.2$ MPa is appropriate for the present cylinder.

Figure 6 reveals that the phase plot of the actuating force F and actuating pressure p_l exists a hysteresis loop. A possible reason for this phenomenon could be attributed to the friction between the piston and wall of the cylinder and the disturbance of the restoring pressure p_r. Taking into consideration the friction and disturbance factors, the actuating force in rise and fall process could be modeled as

$$F_r = (p_l - p_{rr})s - F_{fric} \tag{3}$$

$$F_f = (p_l - p_{rf})s + F_{fric} \tag{4}$$

respectively. Where, F_r and F_f denote the actuating force in rise and fall process respectively. s is pressure action area of the cylinder. F_{fric} denotes the friction between the piston and wall of the cylinder. p_{rr} and p_{rf} denote the restoring pressure in rise and fall process respectively. Combine Eqs. (3) and (4), the gap between the F_r and F_f could be obtained as

$$\Delta F = (p_{rr} - p_{rf})s + 2F_{fric} \tag{5}$$

Equation (5) reveals that the larger friction and disturbance the restoring pressure could aggravate the gap ΔF between F_r and F_f. Therefore, a buffer gas tank with a volume of 350 ml is utilized to reduce the disturbance of the restoring pressure in the present design.

3.3 Non-State-Based Actuating Pressure Modeling. Based on the measured response of the actuating force F and actuating pressure p_l, an approximate model of the actuating pressure p_l could be obtained by model identification as

$$p_l = 5.15 \times 10^{-3} F + 0.19 \tag{6}$$

The obtained approximate model of the actuating pressure p_l is compared to the measured data in Fig. 7(*a*). The modeling error of Eq. (6) is computed and displayed in Fig. 7(*b*). It could be observed that the residual modeling error of Eq. (6) is about −0.027 MPa and 0.027 MPa in the rise and fall process, respectively.

A model verification experiment is then performed to verify the control performance of the identified trajectory model of the actuating pressure p_l. In experiment, the target actuating force increases from 0 N to 50 N at first with a step of 1 N and decreases from 50 N to 0 N subsequently with a step of −1 N. Once the target actuating force F is updated, Eq. (6) will be executed to update the trajectory of the actuating pressure p_l.

The obtained tracking results of Eq. (6) are compared with the reference in Fig. 8. Results reveal that the actuating force could track the reference in general. However, the actuating force control has a remarkable control error over the whole loading and unloading process, which is displayed in Fig. 11. It could be observed that the actuating force control has a maximum error of about −10.1 N. And the error distribution is featured as asymmetric in rise and fall process of the actuating force.

3.4 State-Based Actuating Pressure Modeling. In this section, a state-based model identification method is proposed to achieve a better modeling of the actuating pressure p_l. The proposed state-based model is described as

$$p_l = \begin{cases} p_{lr}(F_r), & F_r = F \cap (\dot{F} \geq 0) \\ p_{lf}(F_f), & F_f = F \cap (\dot{F} < 0) \end{cases} \tag{7}$$

where, p_{lr} and p_{lf} are two independent models of the actuating pressure p_l in rise and fall process. Time derivation of the actuating force $\dot{F}$ denotes the state variable, which could be computed by

$$\dot{F} = F_i - F_{i-1} \tag{8}$$

where subscript i denotes the discrete time series. Based on the measured actuating force F, actuating pressure p_l and state variable $\dot{F}$, the p_{lr} and p_{lf} are identified as

$$p_{lr} = 5.21 \times 10^{-3} F + 0.22 \tag{9}$$

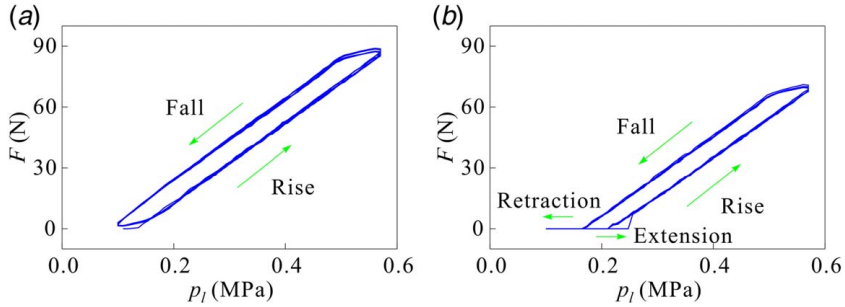

Fig. 6 Measured actuating force F and actuating pressure p_l under different restoring pressure p_r: (*a*) $p_r = 0.1$ MPa and (*b*) $p_r = 0.2$ MPa

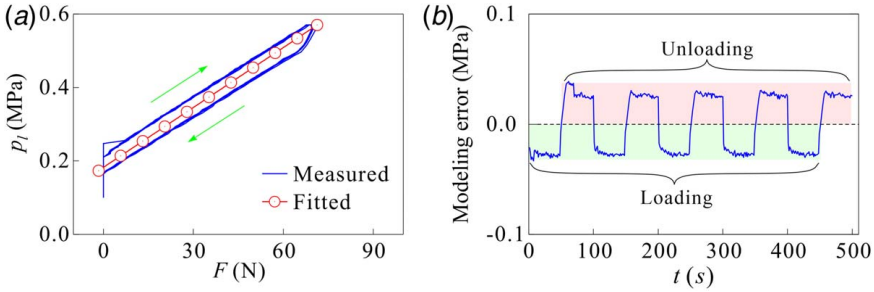

Fig. 7 Non-state-based model of the actuating pressure p_l: (*a*) model identification and (*b*) modeling error

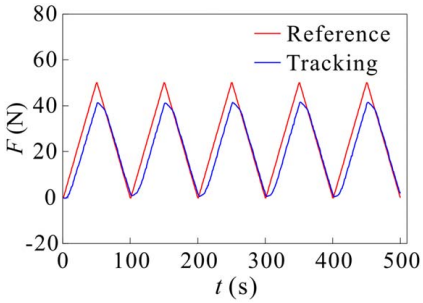

Fig. 8 Experimental verification of the non-state-based model

$$p_{lf} = 5.21 \times 10^{-11} F^6 - 1.45 \times 10^{-8} F^5 + 1.07 \times 10^{-6} F^4 - 3.76 \times 10^{-5} F^3 + 6.28 \times 10^{-4} F^2 + 6.35 \times 10^{-4} F^1 + 0.18 \tag{10}$$

The identified state-based model of the actuating pressure p_l is compared to the measured data in Fig. 9(*a*). The corresponding modeling error is computed and displayed in Fig. 9(*b*). It could be observed that the state-based model of the actuating pressure p_l coincides with the measured data better than that of the non-state-based model, which is shown in Fig. 7(*b*). The state-based model has a maximum modeling error of about −0.017 MPa. Compared with the non-state-based model, the modeling error is reduced by 37.0%

Then a verification experiment is performed to evaluate the control performance of the state-based trajectory model of the actuating pressure p_l. In the experiment, the target actuating force increases from 0 N to 50 N at first with a step of 1 N and decreases from 50 N to 0 N subsequently with a step of −1 N. During the control process, the state variable $\dot{F}$ is computed in real-time. The trajectory of the actuating pressure p_l is generated according to the rules of

$$p_l = \begin{cases} p_{lr} \text{ if } \dot{F} \geq 0 \\ p_{lf} \text{ if } \dot{F} < 0 \end{cases} \tag{11}$$

The obtained tracking results of the state-based model are compared with the reference in Fig. 10. Comparing Figs. 8 and 10, it could be observed that the state-based model of the actuating pressure p_l could achieve a better tracking performance than that of the non-state-based one. The control error of the state-based model is compared with the non-state-based model in Fig. 11. Results reveal that the maximum control error of the state-based model is about −2.3 N. Compared with the non-state-based model, the control error is reduced by about 77.2%.

3.5 Sensor-Less Grasping Control Method. The control structure of the grasping system consists of two layers, those are trajectory planning and actuating layers, as shown in Fig. 12. The trajectory planning layer is utilized to generate the target trajectory of the actuating pressure p_l, it includes two steps: (1) Target actuating force F generation according to Eq. (1), and (2) Target actuating pressure p_l generation according to Eq. (11). According to the computed target actuating force F, the state variable $\dot{F}$ is computed first to determine the trajectory state. Then the target actuating pressure p_l is computed according to Eqs. (9) or (10) based on the state variable $\dot{F}$. Then in actuating layer, the obtained actuating pressure instruction will be executed by the servo valve to actuate the pneumatic cylinder and subsequently the finger mechanism. As the fingertip comes into contact with the object, the grasping force F_g will increase. The servo valve will accomplish the control automatically once the grasping force achieves equilibrium with the target actuating pressure.

4 Experimental Results and Discussion

4.1 Experimental Setup. An experiment platform, as shown in Fig. 13, is established to evaluate the performance of the

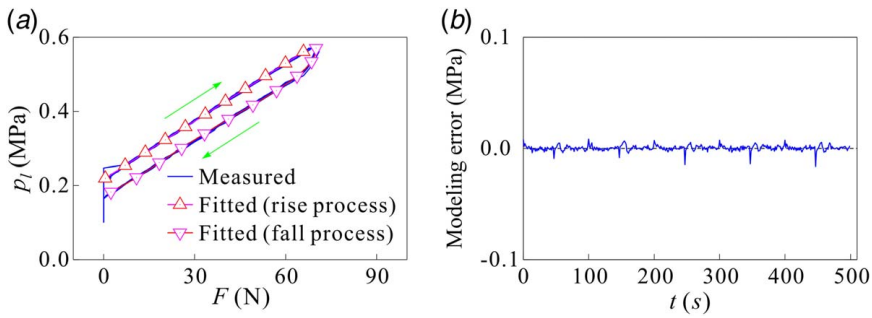

Fig. 9 State-based model of the actuating pressure p_l: (*a*) model identification and (*b*) modeling error

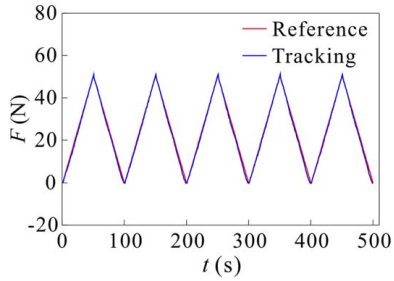

Fig. 10 Experimental verification of the state-based model

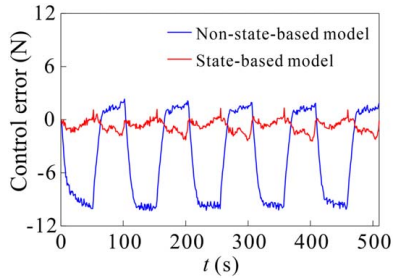

Fig. 11 Control error comparison of the state-based and non-state-based models of the actuating pressure p_l

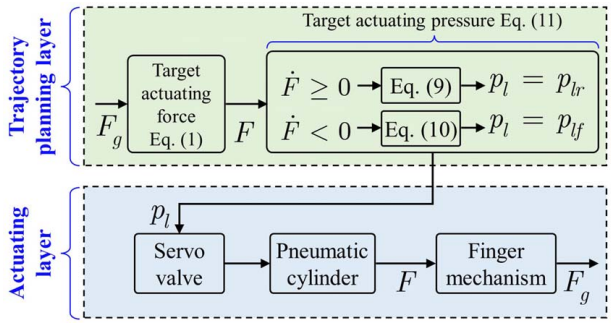

Fig. 12 Control structure of the grasping system

PURG. The hardware composition of the platform is same as the model identification experimental platform, which is shown in Fig. 5, except for the pneumatic cylinder. The pneumatic cylinder in Fig. 5 is replaced as a PURG in the grasping control experiments as shown in Fig. 13. In addition, the force gauge is placed in the grasping range of the finger mechanism to measure the grasping force of the fingertip.

4.2 Grasping Force Control Tests. To evaluate the sensor-less grasping force control performance, the control accuracy and grasping strength control ability are tested in this section.

(1) Grasping force control accuracy tests

As described in Sec. 3, the force transmission ratio between the actuating and grasping space exhibits a nonlinear distribution characteristic with respect to the different configuration of the finger mechanism. To make a comprehensive evaluation, two sets of grasping force control tests are performed under different configurations of the finger mechanism, corresponding grasping range y_g are 56 mm and 87 mm, respectively. The actuating transmission ratio for $y_g = 56$ mm and $y_g = 87$ mm is 0.32 and 0.29, respectively. In sensor-less grasping force control, the target grasping force is set range from 5 N to 10 N with a step of 1 N has been tested.

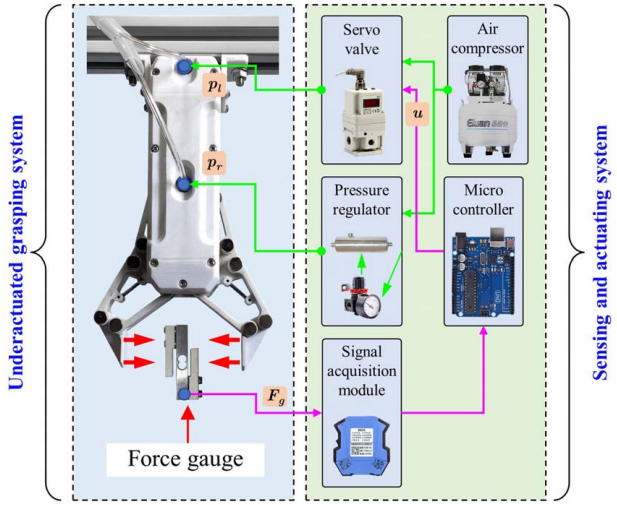

Fig. 13 Experimental platform for the pneumatic underactuated robotic gripper

The measured responses of the grasping force under different control targets and finger mechanism configurations are displayed in Figs. 14 and 15, respectively. From Figs. 14 and 15, it could be observed that the PURG has a rapid grasping speed. The average closing time is about 0.3 s. The corresponding rise time, overshoot, and steady-state error of the grasping force response are summarized in Table 1. Results reveal that the rise time increases as the target grasping force increases. The average value of the rise time is about 0.18 s, and the steady-state error is within the range of −5% to 0%. The resolution of the force control is about 0.3 N. The grasping response of the proposed PURG also exhibits a non-overshoot characteristic as the LSEA-RG [18]. This characteristic could be attributed to the following factors: (1) The actuating medium of the pneumatic cylinder is compressible air, which has an inherent elastic characteristic. During the grasping process, the grasping force will experience a compliant buffer process and reduce the control overshoot. (2) A buffer gas tank has been integrated into the restoring pressure pipeline, which could absorb the dynamic overshoot of the servo valve and improve the control performance. The non-overshoot characteristic of the PURG makes it especially suitable for the grasping of fragile objects, for which the accurate grasping force control is an essential requirement.

It should be noted that the estimation accuracy of the grasping force depends on the actual grasping mode. The present sensor-less grasping control method is suitable for the parallel grasping mode. Through numerical simulation, we have found that the description of the force transmission characteristic under envelope grasping mode is much more complex than the parallel mode. Generally, the actuating force transmission ratio under envelope mode is smaller than that of the parallel one. This means that for the same object, the grasping force under envelope grasping mode will be smaller than that of the parallel one. Therefore, in-depth future research work is required to reveal the coupling mechanism between the actuating and grasping space to model the multi-mode force transmission characteristic and enhance the versatility of the sensor-less grasping control method.

(2) Sensor-less grasping strength control tests

Grasping strength control tests are performed to further evaluate the sensor-less grasping force control ability of the PURG. Figures 16(*a*)–16(*c*) exhibit the parallel grasping process of a dropper under different grasping forces. In Fig. 16(*a*), a 1 N grasping force is utilized to hold the dropper. Then in Fig. 16(*b*), a 2.5 N grasping force is utilized to squeeze the dropper slightly. In Fig. 16(*c*), a 5 N grasping force is applied to the dropper to produce greater extrusion

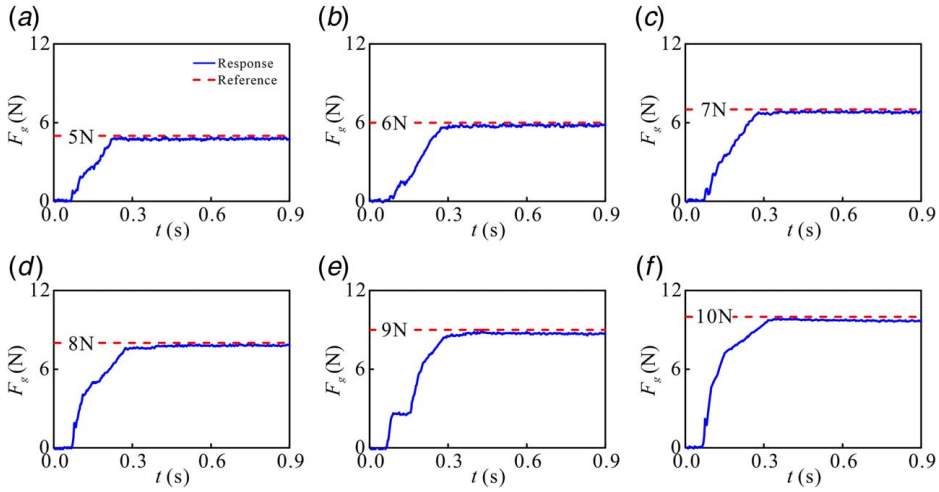

Fig. 14 Grasping force control response for $y_g = 56$ *mm*: (*a*) $F_g = 5$ N, (*b*) $F_g = 6$ *N*, (*c*) $F_g = 7$ *N*, (*d*) $F_g = 8$ *N*, (e) $F_g = 9$ *N*, and (*f*) $F_g = 10$ *N*

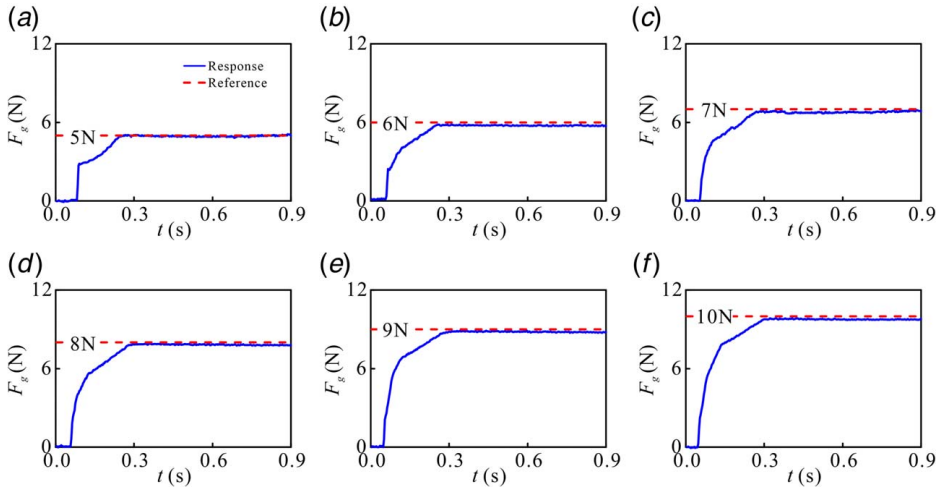

Fig. 15 Grasping force control response for $y_g = 87$ *mm*: (*a*) $F_g = 5$ *N*, (*b*) $F_g = 6$ *N*, (*c*) $F_g = 7$ *N*, (*d*) $F_g = 8$ *N*, (e) $F_g = 9$ *N*, and (*f*) $F_g = 10$ *N*

deformation. Figures 16(*d*) and 16(*e*) exhibit a similar grasping strength control test on a jujube with larger grasping force. The corresponding grasping forces of the Figs. 16(*d*)–16(*f*) are 1 N, 5 N, and 10 N, respectively.

4.3 Sensor-Less Adaptive Grasping Control

(1) Regular and irregular shaped objects grasping

Adaptive grasping experiments are performed to evaluate the sensor-less adaptive grasping performance of the PURG. In experiments, some objects with regular and irregular shapes are tested and the grasping results are shown in Fig. 17. Parallel grasping mode is utilized to grasp the objects with regular shapes, as shown in Figs. 17(*a*)–17(*f*). In Figs. 17(*a*) and 17(*b*), the objects are signature pen and battery with circular grasping surface, respectively. In Figs. 17(*c*)–17(*f*), the objects are staple box, toy dice, pencil sharpener, and toy phone with parallel grasping surface, respectively. In Figs. 17(*g*)–17(*j*), the envelope grasping mode is utilized to grasp the objects with irregular grasping surface, such as screwdriver, glass bottle, water bottle, and toy phone.

(2) Fragile and deformable object grasping

Some fragile and deformable objects are utilized to evaluate the grasping safety of the PURG. In object grasping experiments, the target grasping force is set as 5 N. The grasping results are displayed in Fig. 18. It could be observed that the PURG could grasp the fragile kiwifruit (Fig. 18(*a*)), egg (Fig. 18(*b*)), and deformable milk bottle (Fig. 18(*c*)) safely. Figures 18(*d*) and 18(*e*) display the grasping of soft gloves and deformable color mud, respectively.

(3) Small-sized object grasping

Table 1 Response characteristic of the grasping force control

y_g (mm)	F_g (N)	Rise time (s)	Overshoot (%)	Steady-state error (%)
56	5	0.14	0.0	−4.40
	6	0.17	0.0	−3.50
	7	0.20	0.0	−3.14
	8	0.19	0.0	−2.50
	9	0.20	0.0	−3.44
	10	0.20	0.0	−3.70
87	5	0.14	0.0	−0.80
	6	0.17	0.0	−4.50
	7	0.17	0.0	−2.00
	8	0.18	0.0	−2.63
	9	0.18	0.0	−2.44
	10	0.19	0.0	−2.50

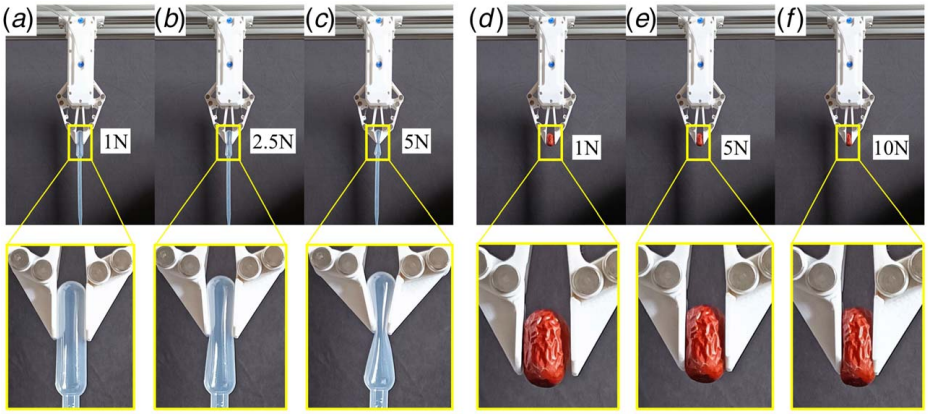

Fig. 16 Grasping strength control tests: (*a*)–(*c*) grasping strength control of a dropper with a grasping force range from 1 N to 5 N, and (*d*)–(*f*) grasping strength control of a jujube with a grasping force range from 1 N to 10 N

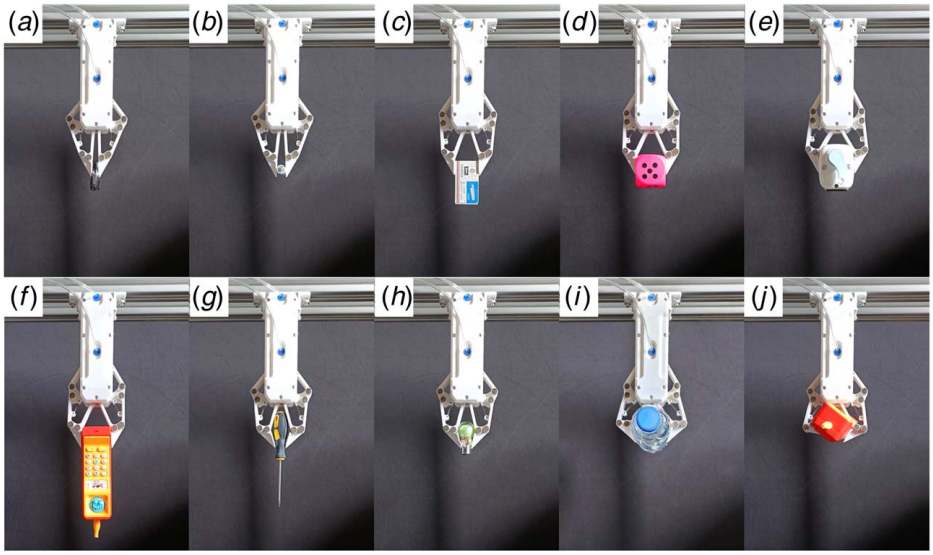

Fig. 17 Adaptive grasping of the regular and irregular shaped objects: (*a*)–(*f*) parallel grasping of the regular shaped objects and (*g*)–(*j*) envelope grasping of the irregular shaped objects

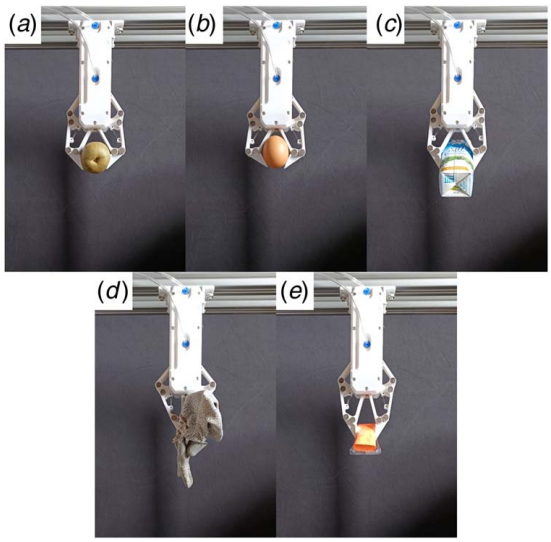

Fig. 18 Adaptive grasping of the fragile and deformable objects: (*a*) deformable and fragile kiwifruit, (*b*) fragile egg, (c) deformable milk box, (*d*) soft fabric gloves, and (e) deformable colored mud

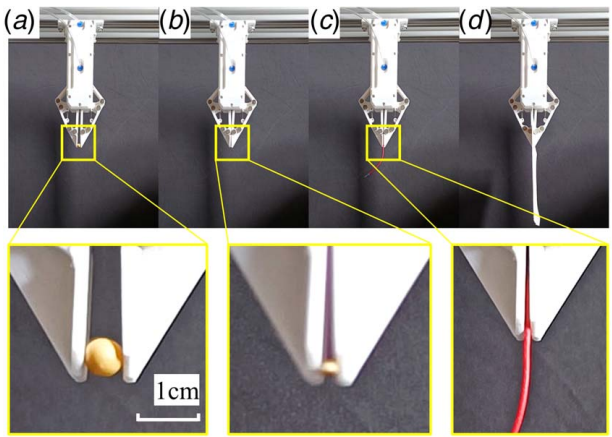

Fig. 19 Precise grasping of the small-sized objects: (*a*) soybean, (*b*) wheat, (c) thin cable, and (*d*) thin-walled paper

Several small-sized objects are utilized to test the precise grasping ability of the PURG as shown in Fig. 19. The object in Figs. 19(*a*)–19(*d*) are soybean, wheat, thin cable, and thin-walled paper. The diameter of the soybean, wheat, and thin cable is 7.3 mm, 2.2 mm, and 1.8 mm, respectively.

5 Conclusion

This study is concerned with the sensor-less grasping force control of a pneumatic underactuated robotic gripper. To achieve above goals, a state-based actuating pressure modeling method and feedforward grasping force control method are proposed. A PURG prototype is fabricated to validate the proposed sensor-less grasping control method experimentally.

Experimental results reveal that the state-based model has a maximum modeling error of about −0.017 MPa. Compared with the non-state-based one, the modeling error could be reduced by 37.0% abruptly. Sensor-less grasping force control experiments are performed to verify the effectiveness of the feedforward grasping force control method. Results reveal that the PURG has a closing time of about 0.3 s. The average value of the rise time of the grasping force control is about 0.18 s, and the steady-state error is within the range of −5% to 0%. This means that the proposed PURG could also exhibit a non-overshoot characteristic as the LSEA-RG [18], which is quite suitable for the situation of non-destructive grasping.

Sensor-less object grasping experiments are performed to evaluate the adaptive grasping performance of the fabricated PURG prototype. Results reveal that the PURG could realize the grasping of regular shaped, irregular shaped, deformable, fragile, and small-size objects to basically fulfill the demands that occurred in real applications.

Acknowledgment

This research is funded by the China Postdoctoral Science Foundation under Grant No. 2022M721613, National Natural Science Foundation of China under Grant Nos. 62273061, 51676099, and Fundamental Research Funds for the Central Universities under Grant No. 30920021104.

Conflict of Interest

There are no conflicts of interest.

Data Availability Statement

The datasets generated and supporting the findings of this article are obtainable from the corresponding author upon reasonable request.

References

[1] Blanes, C., Ortiz, C., Mellado, M., and Beltrán, P., 2015, "Assessment of Eggplant Firmness With Accelerometers on a Pneumatic Robot Gripper," Comput. Electron. Agric., **113**(1), pp. 44–50.

[2] Ji, W., Qian, Z., Xu, B., Chen, G., and Zhao, D., 2019, "Apple Viscoelastic Complex Model for Bruise Damage Analysis in Constant Velocity Grasping by Gripper," Comput. Electron. Agric., **162**(1), pp. 907–920.

[3] Xiong, Y., Peng, C., Grimstad, L., From, P. J., and Isler, V., 2019, "Development and Field Evaluation of a Strawberry Harvesting Robot With a Cable-Driven Gripper," Comput. Electron. Agric., **157**(1), pp. 392–402.

[4] Endo, G., and Otomo, N., 2016, "Development of a Food Handling Gripper Considering an Appetizing Presentation," Proceedings of 2016 IEEE International Conference on Robotics and Automation (ICRA), Stockholm, Sweden, May 16–21, IEEE, pp. 4901–4906.

[5] Wang, Z., and Hirai, S., 2018, "A Soft Gripper With Adjustable Stiffness and Variable Working Length for Handling Food Material," Proceedings of 2018 IEEE International Conference on Real-Time Computing and Robotics (RCAR), Kandima, Maldives, Aug. 1–5, IEEE, pp. 25–29.

[6] Kuriyama, Y., Okino, Y., Wang, Z., and Hirai, S., 2019, "A Wrapping Gripper for Packaging Chopped and Granular Food Materials," Proceedings of 2019 2nd IEEE International Conference on Soft Robotics (RoboSoft), Seoul, South Korea, Apr. 14–18, IEEE, pp. 114–119.

[7] Zhongkui, W., Keung, O., and Shinichi, H., 2020, "A Dual-Mode Soft Gripper for Food Packaging," Rob. Auton. Syst., **125**(1), p. 103427.

[8] Kim, U., Seok, D.-Y., Kim, Y. B., Lee, D.-H., and Choi, H. R., 2016, "Development of a Grasping Force-Feedback User Interface for Surgical Robot System," Proceedings of 2016 IEEE/RSJ International Conference on Intelligent Robots and Systems (IROS), Daejeon, South Korea, Oct. 9–14, IEEE, pp. 845–850.

[9] Gerboni, G., Brancadoro, M., Tortora, G., Diodato, A., Cianchetti, M., and Menciassi, A., 2016, "A Novel Linear Elastic Actuator for Minimally Invasive Surgery: Development of a Surgical Gripper," Smart Mater. Struct., **25**(10), p. 105025.

[10] Guo, J., Low, J.-H., Liang, X., Lee, J. S., Wong, Y.-R., and Yeow, R. C. H., 2019, "A Hybrid Soft Robotic Surgical Gripper System for Delicate Nerve Manipulation in Digital Nerve Repair Surgery," IEEE/ASME Trans. Mechatron., **24**(4), pp. 1440–1451.

[11] Scimeca, L., Maiolino, P., Cardin-Catalan, D., del Pobil, A. P., Morales, A., and Iida, F., 2019, "Non-Destructive Robotic Assessment of Mango Ripeness Via Multi-point Soft Haptics," Proceedings of 2019 International Conference on Robotics and Automation (ICRA), Montreal, QC, Canada, May 20–24, IEEE, pp. 1821–1826.

[12] Seguin, P., Preault, C., Vulliez, P., and Gazeau, J. P., 2023, "Approach for Real In-Hand Dexterity Evaluation: Application to the RoBioSS Hand," ASME J. Mech. Rob., **15**(6), p. 065001.

[13] Odhner, L. U., Jentoft, L. P., Claffee, M. R., Corson, N., Tenzer, Y., Ma, R. R., Buehler, M., Kohout, R., Howe, R. D., and Dollar, A. M., 2014, "A Compliant, Underactuated Hand for Robust Manipulation," Int. J. Rob. Res., **33**(5), pp. 736–752.

[14] Zhang, T., Jiang, L., Wu, X., Feng, W., Zhou, D., and Liu, H., 2014, "Fingertip Three-Axis Tactile Sensor for Multifingered Grasping," IEEE/ASME Trans. Mechatron., **20**(4), pp. 1875–1885.

[15] Jentoft, L. P., Dollar, A. M., Wagner, C. R., and Howe, R. D., 2014, "Intrinsic Embedded Sensors for Polymeric Mechatronics: Flexure and Force Sensing," Sensors, **14**(3), pp. 3861–3870.

[16] Hsu, J., Yoshida, E., Harada, K., and Kheddar, A., 2017, "Self-Locking Underactuated Mechanism for Robotic Gripper," Proceedings of 2017 IEEE International Conference on Advanced Intelligent Mechatronics (AIM), Munich, Germany, July 3–7, IEEE, pp. 620–627.

[17] Kim, U., Lee, D., Yoon, W. J., Hannaford, B., and Choi, H. R., 2015, "Force Sensor Integrated Surgical Forceps for Minimally Invasive Robotic Surgery," IEEE Trans. Rob., **31**(5), pp. 1214–1224.

[18] Hua, H., Liao, Z., and Zhao, J., 2022, "Design, Analysis, and Experiment of an Underactuated Robotic Gripper Actuated by Linear Series Elastic Actuator," ASME J. Mech. Rob., **15**(2), p. 021002.

[19] Hua, H., Liao, Z., and Chen, Y., 2020, "A 1-DOF Bidirectional Graspable Finger Mechanism for Robotic Gripper," J. Mech. Sci. Technol., **34**(11), pp. 4735–4741.

[20] Hua, H., Liao, Z., Wu, X., and Chen, Y., 2021, "A Bezier Based State Calibrating Method for Low-Cost Potentiometer With Inherent Nonlinearity," Measurement, **178**(1), p. 109325.

[21] Hua, H., Song, J., Liao, Z., and Zhao, J., 2022, "Design and Experiment of Miniature Linear Series Elastic Actuator for Robotic Grasping," Trans. Chin. Soc. Agric. Mach., **53**(12), pp. 500–506.

[22] Huang, S.-J., Chang, W.-H., and Su, J.-Y., 2017, "Intelligent Robotic Gripper With Adaptive Grasping Force," Int. J. Control Autom. Syst., **15**(5), pp. 2272–2282.

[23] Guo, M., Wu, P., Yi, B., Gealy, D., McKinley, S., and Abbeel, P., 2019, "Blue Gripper: A Robust, Low-Cost, and Force-Controlled Robot Hand," Proceedings of 2019 IEEE 15th International Conference on Automation Science and Engineering (CASE), Vancouver, BC, Canada, Aug. 22–26, IEEE, pp. 1505–1510.

[24] Hua, H., Liao, Z., Chen, Y., and Xu, C., 2021, "Design and Test of Compact Series Elastic Force Actuator for Grasping Mechanism," Trans. Chin. Soc. Agric. Mach., **52**(12), pp. 426–432.

[25] Hua, H., Liao, Z., Wu, X., Chen, Y., and Feng, C., 2022, "A Back-Drivable Linear Force Actuator for Adaptive Grasping," J. Mech. Sci. Technol., **36**(8), pp. 4213–4220.

[26] Zhou, J., Chen, S., and Wang, Z., 2017, "A Soft Robotic Gripper With Enhanced Object Adaptation and Grasping Reliability," IEEE Rob. Autom. Lett., **2**(4), pp. 1–6.

[27] Gong, Z., Fang, X., Chen, X., Cheng, J., Xie, Z., Liu, J., Chen, B., et al., 2021, "A Soft Manipulator for Efficient Delicate Grasping in Shallow Water: Modeling, Control, and Real-World Experiments," Int. J. Rob. Res., **40**(1), pp. 449–469.

[28] Liu, Q., Liu, A., Meng, W., Ai, Q., and Xie, S. Q., 2017, "Hierarchical Compliance Control of a Soft Ankle Rehabilitation Robot Actuated by Pneumatic Muscles," Front. Neurorobot., **11**(64), p. 64.

[29] Liu, Q., Zuo, J., Zhu, C., and Xie, S. Q., 2020, "Design and Control of Soft Rehabilitation Robots Actuated by Pneumatic Muscles: State of the Art," Future Gener. Comput. Syst., **113**(01), pp. 620–634.

[30] Zhong, B., Cao, J., McDaid, A., Xie, S. Q., and Zhang, M., 2020, "Synchronous Position and Compliance Regulation on a Bi-Joint Gait Exoskeleton Driven by Pneumatic Muscles," IEEE Trans. Autom. Sci. Eng., **17**(4), pp. 2162–2166.

[31] Zhang, B., Xie, Y., Zhou, J., Wang, K., and Zhang, Z., 2020, "State-of-the-Art Robotic Grippers, Grasping and Control Strategies, as Well as Their Applications in Agricultural Robots: A Review," Comput. Electron. Agric., **177**(1), pp. 1–20.

[32] Aschemann, H., and Schindele, D., 2014, "Comparison of Model-Based Approaches to the Compensation of Hysteresis in the Force Characteristic of Pneumatic Muscles," IEEE Trans. Ind. Electron., **61**(7), pp. 3620–3629.

[33] Huang, M., Lu, Q., Chen, W., Qiao, J., and Chen, X., 2019, "Design, Analysis, and Testing of a Novel Compliant Underactuated Gripper," Rev. Sci. Instrum., **90**(4), p. 045122.

[34] Birglen, L., and Gosselin, C., 2004, "Optimal Design of 2-Phalanx Underactuated Fingers," Proceedings of IMG2004: IEEE International Conference on Intelligent Manipulation and Grasping, Hong Kong, China, Sept. 28–Oct. 2, pp. 110–116.

[35] Ballesteros, J., Pastor, F., GómezDeGabriel, J. M., Gandarias, J. M., and Urdiales, C., 2020, "Proprioceptive Estimation of Forces Using Underactuated Fingers for Robot-Initiated pHRI," Sensors, **20**(10), pp. 1–13.

[36] Andrés, F. J., Pérez-González, A., Rubert, C., Fuentes, J., and Sospedra, B., 2018, "Comparison of Grasping Performance of Tendon and Linkage Transmission Systems in an Electric-Powered Low-Cost Hand Prosthesis," ASME J. Mech. Rob., **11**(1), p. 011018.

[37] Shin, Y. J., Lee, H. J., Kim, K.-S., and Kim, S., 2012, "A Robot Finger Design Using a Dual-Mode Twisting Mechanism to Achieve High-Speed Motion and Large Grasping Force," IEEE Trans. Rob., **28**(6), pp. 1398–1405.

[38] Zhang, T., Jiang, L., and Liu, H., 2012, "A Novel Grasping Force Control Strategy for Multi-fingered Prosthetic Hand," J. Cent. South Univ., **19**(6), pp. 1537–1542.

[39] Memar, A. H., and Esfahani, E. T., 2020, "A Robot Gripper With Variable Stiffness Actuation for Enhancing Collision Safety," IEEE Trans. Ind. Electron., **67**(8), pp. 6607–6616.